Atom-Based Radio-Frequency Field Calibration and Polarization Measurement Using Cesium nD_J Floquet States

Yuechun Jiao,[1,3] Liping Hao,[1,3] Xiaoxuan Han,[1,3] Suying Bai,[1,3] Georg Raithel,[1,2,*] Jianming Zhao,[1,3,†] and Suotang Jia[1,3]

[1]*State Key Laboratory of Quantum Optics and Quantum Optics Devices, Institute of Laser Spectroscopy, Shanxi University, Taiyuan 030006, China*

[2]*Department of Physics, University of Michigan, Ann Arbor, Michigan 48109-1120, USA*

[3]*Collaborative Innovation Center of Extreme Optics, Shanxi University, Taiyuan 030006, China*

(Received 1 March 2017; revised manuscript received 26 May 2017; published 24 July 2017)

We investigate atom-based electric-field calibration and polarization measurement of a 100-MHz linearly polarized radio-frequency (rf) field using cesium Rydberg-atom electromagnetically induced transparency in a room-temperature vapor cell. The calibration method is based on matching experimental data with the results of a theoretical Floquet model. The utilized $60D_J$ fine-structure Floquet levels exhibit J- and m_j-dependent ac Stark shifts and splittings, and they develop even-order rf-modulation sidebands. The Floquet map of cesium $60D_J$ fine-structure states exhibits a series of exact crossings between states of different m_j's which are not rf coupled. These exact level crossings are employed to perform a rapid and precise ($\pm 0.5\%$) calibration of the rf electric field. We also map out three series of narrow avoided crossings between fine-structure Floquet levels of equal m_j's and different J's, which are weakly coupled by the rf field via a Raman process. The coupling leads to narrow avoided crossings that can also be applied as spectroscopic markers for rf-field calibration. We further find that the line-strength ratio of intersecting Floquet levels with different m_j's provides a fast and robust measurement of the rf field's polarization.

DOI: 10.1103/PhysRevApplied.8.014028

I. INTRODUCTION

In recent decades, atom-based metrology has had an enormous impact on science, technology, and everyday life. Seminal advances include microwave and optical atomic clocks [1,2], the Global Positioning System, and highly sensitive, position-resolved magnetometers [3,4]. Atom-based field measurement has clear advantages over other field measurement methods because it is calibration-free, due to the invariance of atomic properties. Atom-based metrology has recently expanded into electric-field measurement.

An all-optical sensing approach employed by numerous groups is electromagnetically induced transparency (EIT) of atomic vapors, utilizing Rydberg levels [5] to measure the properties of the electric field. Rydberg atoms are well suited for this purpose owing to their extreme sensitivities to dc and ac electric fields, which manifest in large dc polarizabilities and microwave-transition dipole moments [6]. Developments include measurements of microwave fields [7,8] and polarizations [9,10], millimeter waves [11], static electric fields [12], and subwavelength imaging of microwave electric-field distributions [13,14].

In the frequency range from 10s to 100s of megahertz, Rydberg-EIT rf-modulation spectroscopy is a promising method for accomplishing an atom-based, calibration-free rf electric-field measurement [15,16]. Rydberg EIT in vapor cells [17,18] and in hollow-core fibers [19] offers significant potential for miniaturization of the rf sensor.

Accurate calibration of the electric field is important, for instance, for antenna calibration, characterization of electronic components, etc. Conventional calibration with field sensors that involve dipole antennas (which need to be calibrated first) obviously leads to a chicken-and-egg dilemma [20]. In this work, we provide an atom-based calibration method for vector electrometry of rf fields using Rydberg EIT in cesium vapor cells. The basic idea is that the rf generates a series of intersections between levels in the Rydberg Floquet map (a map in which field-perturbed Floquet level energies are plotted versus the rf electric field). The (anti)crossings occur between Floquet states originating in fine-structure components of nL_J states with equal principal and angular-momentum quantum numbers n and L. The crossings present excellent field markers that we use as calibration points for the electric-field strength. Specifically, we measure the rf-dressed Cs $60D_J$ states via Rydberg-EIT spectroscopy at a test frequency of 100 MHz. The dependence of the Floquet spectrum on the strength and the polarization of the rf field is investigated. There are exact crossings between different states of m_j, $1/2$, $3/2$, and $5/2$, which are not coupled in a linearly polarized rf field. The crossings provide field markers, which we use to calibrate the field strength in a test rf transmission system. We also analyze narrow, spectroscopically resolved

*Corresponding author.
graithel@umich.edu
†Corresponding author.
zhaojm@sxu.edu.cn

anticrossings between Floquet states of the same m_j, $1/2$ (or $3/2$), and different J's, $3/2$ and $5/2$. Transitions between those states are allowed via a rf Raman process. Furthermore, the EIT line-strength ratios of intersecting Floquet states with different m_j's yield the field polarization. At various stages of our work, the measured spectroscopic data are matched with the results of Floquet calculations to accomplish the calibration tasks.

In comparison with antenna-based techniques for rf electric-field measurement, atom-based spectroscopic field measurement holds promise for wire- and contact-free, all-optical rf-field analysis, in a manner that removes the need for sensor calibration. The results for field-polarization-dependent line-strength ratios can lead to a convenient method to determine rf-field polarization. In the future, atom-based rf-field probes may enable rapid and robust rf-field and polarization measurements.

II. EXPERIMENTAL SETUP

A schematic of the experimental setup and the relevant Rydberg three-level ladder diagram are shown in Figs. 1(a) and 1(b). The experiments are performed in a cylindrical room-temperature cesium vapor cell that is 50 mm long and that has a 20-mm diameter. The cell is suspended between two parallel aluminum plate electrodes that are separated by $d = 28$ mm. The EIT coupling-laser and probe-laser beams are overlapped and counterpropagated along the centerline of the cell (propagation direction along the $\hat{z}$ axis). The coupling and probe lasers have the same linear polarization in the x-y plane. The angle θ between the laser polarizations and the rf field (which points along the $\hat{y}$ axis) is varied by rotating the polarization of the laser beams with $\lambda/2$ plates, as seen in Fig. 1(a). The weak EIT probe beam (central Rabi frequency $\Omega_p = 2\pi \times 9.2$ MHz and $1/e^2$ waist $w_0 = 75$ μm) has a wavelength $\lambda_p = 852$ nm, and it is frequency locked to the transition $|6S_{1/2}, F = 4\rangle \rightarrow |6P_{3/2}, F' = 5\rangle$, as shown in Fig. 1(b). The coupling beam (central Rabi frequency $\Omega_c = 2\pi \times 7.2$ MHz for $60D_{5/2}$ and $1/e^2$ waist $w_0 = 95$ μm) is provided by a commercial laser (Toptica TA-SHG110), has a wavelength of 510 nm and a linewidth of 1 MHz, and is scanned over a range of 1.5 GHz through the $|6P_{3/2}, F' = 5\rangle \rightarrow |nD_J\rangle$ Rydberg transition. The EIT signal is observed by measuring the transmission of the probe laser using a photodiode (PD) after a dichroic mirror (DM). An auxiliary rf-free EIT reference setup [not shown, but similar to the one sketched in Fig. 1(a)] is operated with the same lasers as the main setup. The auxiliary EIT signal is employed to locate the 0-detuning frequency reference point for all EIT spectra that we show; it allows us to correct for small frequency drifts of the coupling laser.

The rf voltage amplitude, V, provided by a function generator (Tektronix AFG3102), is applied to the electrodes as shown in Fig. 1(a), and the rf electric-field vector, $\mathbf{E}$, points along $\hat{y}$ [the blue arrow in Fig. 1(a)]. The rf frequency is fixed,

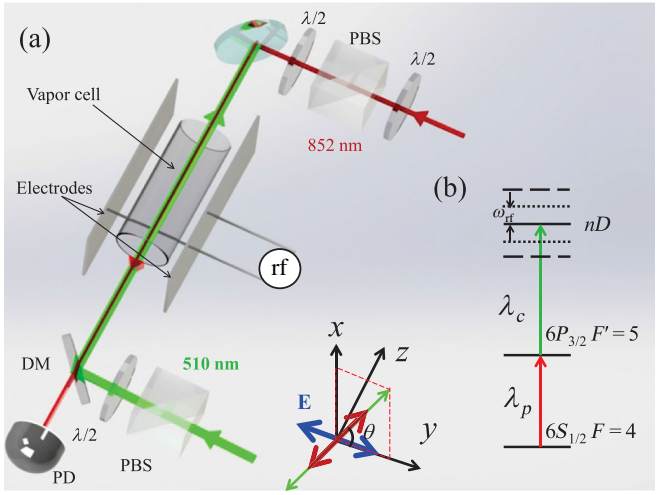

FIG. 1. (a) Schematic of the experimental setup. The coupling and probe beams counterpropagate through a cesium vapor cell along the $\hat{z}$ axis. Two electrode plates are located on both sides of the vapor cell, where the rf field is applied. The polarization of the rf field $\mathbf{E}$ (the blue arrow) points along the $\hat{y}$ axis. The polarization of the beams (the red and green arrows) can be adjusted with the $\lambda/2$ wave plates to form an angle θ with the rf electric field $\mathbf{E}$. The probe beam is passed through a dichroic mirror (DM) and is detected with a photodiode (PD). Polarizing beam splitters (PBS) are used to produce beams with pure linear polarizations. (b) Energy-level scheme of cesium Rydberg-EIT transitions. The probe laser, λ_p, is resonant with the lower transition, $|6S_{1/2}, F = 4\rangle \rightarrow |6P_{3/2}, F' = 5\rangle$, and the coupling laser, λ_c, is scanned through the Rydberg transitions $|6P_{3/2}, F' = 5\rangle \rightarrow |60D_J\rangle$. The applied rf electric field (frequency $\omega_{\rm rf} = 2\pi \times 100$ MHz) produces ac Stark shifts and rf-modulation sidebands that are separated in energy by even multiples of $\hbar\omega_{\rm rf}$.

$\omega_{\rm rf} = 2\pi \times 100$ MHz, and the rf-field amplitude, E, is varied by changing V. The rf-field ac shifts the Rydberg levels and generates even-order modulation sidebands [see Fig. 1(b)]. The rf-field amplitude E is approximately uniform within the atom-field interaction volume. Using a finite-element calculation, we determine that the average electric field in the atom-field interaction region is 95% of the field that would be present absent the dielectric glass cell (i.e., the glass shields 5% of the field). The glass cell further gives rise to an approximately $\pm 1.5\%$ field inhomogeneity along the beam paths within the cell.

The rf transmission line between the source and the cell has unavoidable standing-wave effects. While the standing-wave effect is hard to model due to the details of the experimental setup, which are fairly complex from the viewpoint of rf-field modeling, the setup still constitutes a linear transmission system. Therefore, for any given frequency and fixed arrangement of the wiring and the electromagnetic boundary conditions, the magnitude of the voltage amplitude that occurs on the rf-field plates follows $V_C = tV$, where t is a frequency-dependent transmission factor that is specific to the details of the rf

transmission line. As discussed in detail in Sec. III, we use the atom-based field measurement method to determine the transmission factor to be $t = 1.326 \pm 0.007$. The average rf electric-field amplitude, E, averaged over the atom-field interaction zone inside the cell, is then related to the known voltage amplitude, V, generated by the source via $E = (V_C/d) \times 0.95 = (V/d) \times 0.95 \times t$ (d is the distance between the field plates). In this relation, the only factor that is difficult to determine is the transmission factor t [21]. The experiment described in this paper represents a good example of how the atom-based field measurement method allows one to measure t and to thereby calibrate rf electric fields.

III. RYDBERG-ATOM-BASED CHARACTERIZATION OF A RF FIELD

A. Electric-field calibration

In Fig. 2, we show Rydberg-EIT spectra for the $60D_J$ states for $\theta = 30°$ without a rf field (the bottom curve) and with the indicated rf fields (the upper-two curves). The bottom EIT spectrum is obtained with the rf-free reference setup. The $60D_{5/2}$ main peak in the reference spectrum defines the 0-detuning position. Since the value of the $60D_J$ fine-structure splitting (the 318-MHz arrow in Fig. 2) is well known, the spacing between the zero-field $60D_J$ fine-structure components is used to calibrate the detuning axis. The top-two curves show EIT spectra for applied rf-field strengths $E = 0.252$ V/cm and 0.504 V/cm. The $E = 0.252$ V/cm plot illustrates the rf-induced ac Stark shifts in weak rf fields. The degeneracy between the $m_j = 1/2$, $3/2$, and $5/2$ magnetic substates of the $60D_J$ levels becomes lifted. [The quantization axis for m_j is the direction of **E** in Fig. 1(a).] Since the rf-field frequency is much lower than the Kepler frequency (35 GHz for Cs $60D$), the ac shifts in weak rf fields are nearly identical to $-\alpha_{\rm dc}E^2_{\rm rms}/2$, where $\alpha_{\rm dc}$ represents the dc polarizabilities of the $|60D_J, m_j\rangle$ states, and $E_{\rm rms} = E/\sqrt{2}$ is the rf root-mean-square field. This approximate identity has been verified with a dc Stark shift calculation (not shown). At higher fields, rf-induced even-harmonic sidebands for $N = \pm 2, \pm 4$ appear; they are marked with magenta circles in the top curve of Fig. 2. The sidebands come in pairs: the lower-frequency component has $m_j = 3/2$, the higher-frequency one $m_j = 1/2$. The lines that do not shift much throughout Fig. 2 are the $|60D_J, m_j = J\rangle$ states; these states have near-zero polarizability. The ac shifts and sideband separations are on the same order as the fine-structure splitting of $60D_J$. This similarity in energy scales is important because it gives rise to the level crossings in the Floquet maps discussed below.

We perform a series of measurements such as in Fig. 2 over an E-field range of 0–0.76 V/cm, in steps of 0.006 V/cm. We assemble the rf-EIT spectra in a

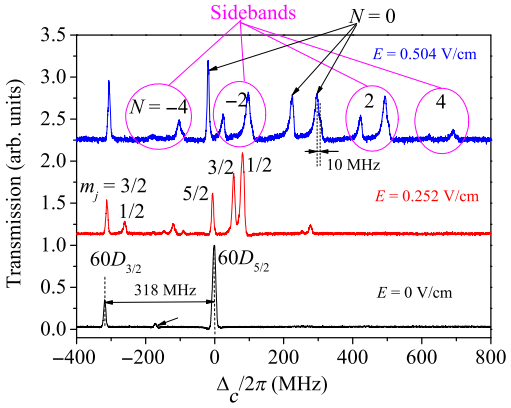

FIG. 2. Measured Rydberg-EIT spectra for an applied rf field with $\omega_{\rm rf} = 2\pi \times 100$ MHz and the indicated amplitudes $E = 0$ V/cm (bottom curve), 0.252 V/cm (middle curve), and 0.504 V/cm (top curve), respectively. The main peak at 0 detuning in the field-free spectrum corresponds to the $|6S_{1/2}F = 4\rangle \rightarrow |6P_{3/2}F' = 5\rangle \rightarrow |60D_{5/2}\rangle$ cascade EIT. The small peak at −168 MHz (the small arrow) originates in the intermediate-state hyperfine level $|6P_{3/2}, F' = 4\rangle$ [16]. The peak at −318 MHz is the $60D_{3/2}$ EIT line. The peaks within the magenta circles are rf-induced sidebands of the indicated orders.

Floquet map, shown in Fig. 3. At fields $E \lesssim 0.2$ V/cm, the m_j sublevels shift and split due to the m_j-dependent quadratic ac Stark effect. The even-harmonic level-modulation sidebands, labeled $N = \pm 2$, ± 4, begin to appear when the rf field is increased further (also see Refs. [15,16]). To match the measured EIT spectra with theory, we numerically calculate Rydberg-EIT spectra using Floquet theory, with the results shown by semitransparent overlaid symbols in Fig. 3. For details of the Floquet calculation, see Refs. [16,22,23].

A central point of this work is that the $|60D_{5/2}, m_j = 5/2\rangle$ level, which has a near-zero polarizability and ac Stark shift, undergoes a series of crossings with the $m_j = 1/2$, $3/2$ modulation sidebands. The crossings are exact because the linearly polarized rf field does not mix quantum states of different m_j's. The crossings can be measured with about 1% precision. As an example, in Fig. 3, we show an enlargement of the first level crossing. The crossing is centered at $E_1 = 0.390$ V/cm, with an estimated uncertainty of ± 0.004 V/cm, corresponding to a relative uncertainty of $\pm 1\%$. The uncertainty is mostly attributed to the intrinsic EIT linewidth, which increases with increasing coupling and probe Rabi frequencies. Laser linewidths and interaction-time broadening also contribute to the observed linewidths.

In Fig. 3, six such crossings are visible within the rectangular box. With the rf-source voltage amplitudes V_i at which the crossings are observed, and recalling that the glass cell shields 5% of the electric field from the atoms, the electric field the atoms would experience for an amplitude transmission factor of 1 would be $E_{0,i} = 0.95 \times V_i/d$.

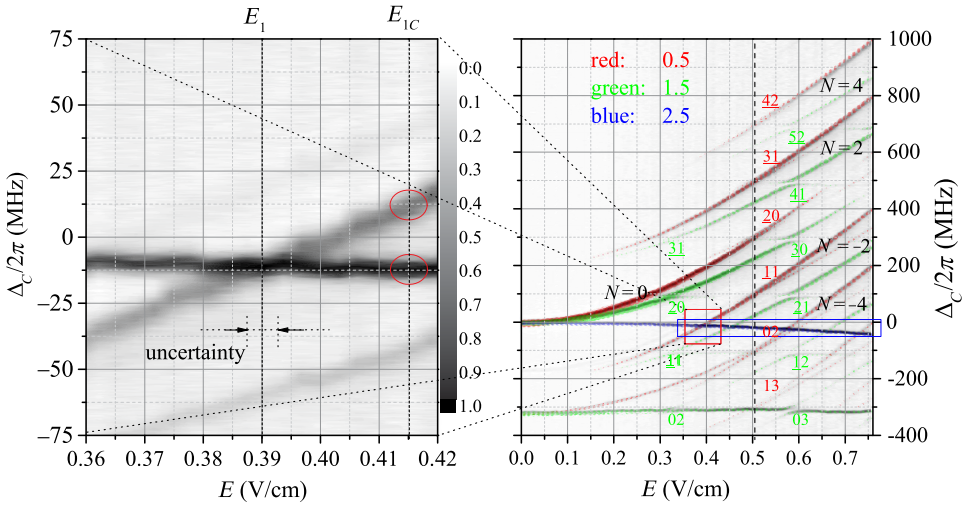

FIG. 3. Measurement of a Cs $60D_J$ Floquet map for $\theta = 30°$ as a function of rf electric field E with $\omega_{\rm rf} = 2\pi \times 100$ MHz, with calculated Floquet maps displayed as overlaid semitransparent symbols. Experimental EIT line strength is displayed on a linear gray scale. The areas of the semitransparent symbols are proportional to the calculated EIT line strength. As the field strength increases, the levels $|60D_J, m_j\rangle$ become ac shifted with m_j-dependent polarizabilites, and even level-modulation sidebands appear. The N labels show sideband orders of the $|60D_{5/2}, m_j = 1/2, 3/2\rangle$ states. The $|60D_{5/2}, m_j = 5/2\rangle$ state has near-zero polarizability and crosses with several $m_j = 3/2, 1/2$ bands. These crossings are used for atom-based rf-field calibration (see the text). The panel on the left shows an enlargement of the crossing at $E_1 = 0.390$ V/cm, indicated by the red square. The labels of the avoided crossings are explained in the text. The rectangular box encloses the six level crossings we use for field calibration.

The ratios between the known (theoretical) electric fields where the crossings actually occur, E_i, and $E_{0,i}$ yield six readings for the amplitude transmission factor, $t_i = E_i/E_{0,i}$. In Table I it is seen that the t_i's have a very small spread and do not exhibit a systematic trend from low to high field. The average, $t = 1.326 \pm 0.007$, is the desired calibration factor for the experimental electric-field axis. The x-axis in Fig. 3 shows the calibrated experimental electric field, $E = tE_0 = t \times 0.95 \times V/d$, with voltage amplitude V at the source. The overall relative uncertainty of the atom-based rf-field calibration performed in this experiment is $\pm 0.5\%$, similar to what was obtained in Ref. [24] and about an order of magnitude better than in traditional rf-field calibrations [25,26]. The use of narrow-band coupling and probe lasers, lower Rabi frequencies, and larger-diameter laser beams is expected to reduce the uncertainty to considerably smaller values.

TABLE I. The columns show, in order, the crossing number, the calculated electric field E for the crossing, the experimental electric field $E_0 = 0.95 \times V/d$ the atoms would be exposed to for a rf amplitude transmission factor $t = 1$, and the transmission factor $t = E/E_0$.

Crossing no. i	E_i (V/cm)	$E_{0,i}$ (V/cm)	t_i
1	0.390	0.2964	1.3158
2	0.457	0.3449	1.3252
3	0.576	0.4323	1.3326
4	0.594	0.4456	1.3332
5	0.657	0.4978	1.3198
6	0.732	0.5510	1.3285

We note that the calibration uncertainty achieved in this work is based on matching experimental and calculated spectroscopic data at the locations of a series of six isolated level crossings that all occur within a narrow spectral range of less than 50-MHz width (see the rectangular box in Fig. 3). Hence, a fairly small amount of spectroscopic data suffices for the presented atom-based rf-field calibration. From Fig. 3, it is obvious that this advantage traces back to a specific feature of cesium nD_J states, namely, that these states offer a mix of magnetic sublevels with near-zero and large ac polarizabilities. rf-dressed Rydberg-EIT spectra of rubidium atoms do not present a similar advantage [24].

In Fig. 3, we further observe three series of avoided crossings, which are due to a rf sideband of the $J = 3/2$ level intersecting with a rf sideband of the $J = 5/2$ level. The first number in the avoided-crossing labels shows the number of rf photon pairs taken from the rf field to access the $J = 3/2$ band, while the second shows the number of rf photon pairs taken from the rf field to access the $J = 5/2$ band. Negative rf photon numbers, indicated by underbars, correspond to stimulated rf photon emission. The coupling between the intersecting $J = 3/2$ and $J = 5/2$ bands is a two-rf-photon Raman process in which the atom absorbs and reemits a rf photon while changing J from 3/2 to 5/2, or vice versa. This is a second-order electric-dipole transition, which, for the given polarization, has selection rules $\Delta L = 0$, 2 and $\Delta m_j = 0$. In Fig. 3, three series of avoided crossings that satisfy these selection rules are

visible, one for $m_j = 1/2$ and two for $m_j = 3/2$. Each series has a fixed E value and consists of copies of the same avoided crossing along the Δ_c axis, in steps of 200 MHz. The $m_j = 3/2$ series is particularly easy to spot because one of the two intersecting Floquet states has near-zero polarizability. The Raman coupling causing the avoided crossings equals the minimal avoided-crossing gap size. For a fixed Floquet-state wave function, the Raman coupling strength should scale as E^2. For the $m_j = 3/2$ avoided crossings at 0.319 V/cm, we observe a coupling strength of 8.6 MHz, while those at 0.579 V/cm have a coupling strength of 19.3 MHz. The coupling-strength ratio, which is 2.2, is somewhat smaller than the E^2 ratio, which is 3.3. The deviation indicates a moderate variation of the Floquet-state wave functions between 0.319 and 0.579 V/cm (which is expected).

From a field-calibration point of view, the avoided crossings and other details in the spectra could be used to further reduce the uncertainty in the atom-based rf-field calibration factor t, which is planned for future work. Comparing the cesium and rubidium level structures, it is again noteworthy that cesium offers a combination of m_j-dependent polarizabilities that is particularly favorable for this purpose.

In the top curve in Fig. 2, it is noted that the $|60D_{5/2}, m_j = 5/2\rangle$ and $|60D_{3/2}, m_j = 3/2\rangle$ Floquet states are narrow and symmetric, whereas the other Floquet lines are much wider and are asymmetrically broadened. Furthermore, the $m_j = 1/2$ lines exhibit a shoulder on the high-frequency side (see the marker equal to approximately 10 MHz in Fig. 2), while the $m_j = 3/2$ lines have no shoulder. The scan shown in the top curve of Fig. 2 also corresponds to the vertical dashed line near 0.5 V/cm in Fig. 3. A close inspection and a comparison of Figs. 3 and 2 (top curve) reveal that the shoulders of the $m_j = 1/2$ lines are due to the series of narrow avoided crossings between Floquet states in the $m_j = 1/2$ manifold. The shoulders correspond to the weaker, higher-frequency component of the crossing. The asymmetric line broadening of the wide lines is due to the 3% full-width variation of the rf field within the atom-field interaction zone. For instance, for the $m_j = 3/2$ lines we estimate an inhomogeneous linewidth of $\Delta W = 3\%E[(dW)/dE] \approx 13$ MHz, which is close to the observed width of about 15 MHz. (The $m_j = 1/2$ lines in the top curve of Fig. 2 are also inhomogeneously broadened, but we do not give a broadening estimate for those lines because of the interference with the mentioned avoided crossing.)

B. rf polarization measurement

Rydberg-EIT spectra generally depend on the laser polarizations [27,28]. This fact also applies to rf-modulated Rydberg-EIT spectra. Here, we study the dependence of line-strength ratios on the angle θ between the rf field and the polarization of the laser beams (both laser beams are linearly polarized, and the polarizations are parallel to each other; see Fig. 1). For a line-strength comparison of Floquet levels with different m_j's, it is advantageous to choose an electric field close to one of the exact crossings discussed above because the two lines of interest will then appear in close proximity to each other, allowing for a rapid measurement. Additionally, since states with different m_j's do not mix, the line-strength measurements are robust against small variations of the rf electric field. As an example, we show in the Fig. 4 inset the rf-EIT spectra for $\theta = 30°$ (the lower curve) and 60° (the upper curve) at a rf field $E_{1C} = 0.415$ V/cm, marked with a dashed line in the left panel of Fig. 3. The two peaks labeled $A1$ and $A2$ within the blue square in the Fig. 4 inset correspond to the Floquet levels marked with red circles in Fig. 3. The peak $A1$, which corresponds to the $N = 0$ rf band of the $|J = 5/2, m_j = 5/2\rangle$ Floquet state, increases with the angle θ, whereas the peak $A2$, which corresponds to the $N = -2$ rf band of the $|J = 5/2, m_j = 1/2\rangle$ state, decreases with θ. To quantify this polarization-angle dependence, we introduce the parameter $A(\theta) = (A1 - A2)/(A1 + A2)$, where $A1$ and $A2$ represent the respective areas of Gaussian peaks obtained from double-Gaussian fits to the spectra at angle θ. Since the intersecting lines have different differential dipole moments, it is important to use the areas and not the peak heights (see the discussion in the last paragraph of Sec. III A). Figure 4 shows A as a function of the θ at $E_{1C} = 0.415$ V/cm for the indicated probe-laser Rabi frequencies, together with the corresponding line-strength ratio obtained from Floquet calculations (the Floquet calculation yields line strengths valid for the case of low saturation, $\Omega_p < \Gamma_2 = 2\pi \times 5.2$ MHz). We find excellent agreement between the measurements and calculations for $\Omega_p = 2\pi \times 9.2$ MHz. Curves such those as in Fig. 4 can be

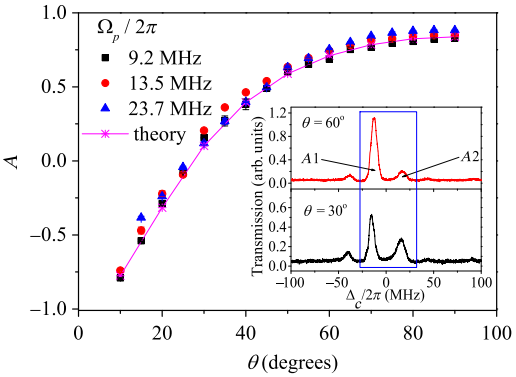

FIG. 4. Experimental data (the symbols) and calculations (the line) for the line-strength ratio $A = (A1 - A2)/(A1 + A2)$ defined in the text at a rf field of $E_{1C} = 0.415$ V/cm, as a function of the polarization angle θ. The data are for the indicated values of the probe Rabi frequency. (Inset) Sample EIT spectra for $\theta = 30°$ and 60° and $\Omega_p/2\pi = 9.2$ MHz.

used to measure the polarization of a rf field with unknown linear polarization. The angle uncertainty can be estimated as $\Delta\theta = |\Delta A|/[(dA)/d\theta]$, where ΔA is the difference between experimental and calculated values of $A(\theta)$, and $[(dA)/d\theta]$ is the derivative of the calculated curve. For the lowest-power case in Fig. 4, a straightforward analysis shows angle uncertainties below 2° for $\theta < 60°$. In the domain $60° < \theta < 90°$, the angle uncertainty gradually increases from 2° to 7° because the derivative becomes small. We note that this method of polarization measurement has the advantage of being both simple and very fast since the areas of only two lines need to be measured. At the expense of reduced acquisition speed, the uncertainty could be improved by measuring line-strength ratios of multiple line pairs and by averaging over a number of spectra.

The data for higher probe Rabi frequencies in Fig. 4 show a more significant deviation from the calculated curve. This result is not unexpected because the calculation is for negligible saturation of the probe transition, whereas the experimental data in Fig. 4 vary between moderate and strong saturation of the probe transition. In addition to saturation broadening effects, there may also be optical-pumping effects [29] that could affect the line-strength ratio. This issue is beyond the scope of the present work.

IV. CONCLUSION

In this paper, we demonstrate a rapid and robust atom-based method to calibrate the electric field and to measure the polarization of a 100-MHz rf field, using Rydberg EIT in a room-temperature cesium vapor cell as an all-optical field probe. The EIT spectra exhibit rf-field-induced ac Stark shifts, splittings, and even-order level-modulation sidebands. A series of exact Floquet-level intersections that are specific to cesium Rydberg atoms are used for calibrating the rf electric field with an uncertainty of ±0.5%. The dependence of the Rydberg-EIT spectra on the polarization angle of the rf field is studied. Our analysis of certain line-strength ratios leads to a convenient method for determining the polarization of the rf electric field. The Rydberg-EIT spectroscopy presented here could be applied to atom-based, antenna-free calibration of rf electric fields and polarization measurement. It is anticipated that an extended analysis of all exact and avoided crossings, as well as other spectroscopic features, will significantly lower the calibration uncertainty. Future work involving narrow-band laser sources, miniature spectroscopic cells as well as improved spectroscopic methods (lower Rabi frequencies, wider probe and coupler beams) are expected to further reduce the calibration uncertainty.

The atom-based field measurement method as a whole is of current interest to national metrology labs, e.g., NIST and NIM, because it paves the way towards defining fields through calibration-free, invariable atomic properties [30]. Since the Rydberg-EIT rf-field measurement method employs small room-temperature vapor cells, as opposed to vacuum chambers and cold-atom setups, it may be applicable to atom-based rf-field testing and measurement.

ACKNOWLEDGMENTS

The work was supported by the National Key R&D Program of China (Grant No. 2017YFA0304203), the National Natural Science Foundation of China (Grants No. 11274209, No. 61475090, and No. 61675123), Changjiang Scholars and Innovative Research Team in University of Ministry of Education of China (Grant No. IRT13076), the State Key Program of National Natural Science of China (Grant No. 11434007), and a research project supported by Shanxi Scholarship Council of China (Grant No. 2014-009). G. R. acknowledges support from the National Science Foundation (Grant No. PHY-1506093) and the BAIREN plan of Shanxi province.

[1] T. P. Heavner, E. A. Donley, F. Levi, G. Costanzo, T. E. Parker, J. H. Shirley, N. Ashby, S. Barlow, and S. R. Jefferts, First accuracy evaluation of NIST-F2, Metrologia **51**, 174 (2014).

[2] A. D. Ludlow, M. M. Boyd, Jun Ye, E. Peik, and P. O. Schmidt, Optical atomic clocks, Rev. Mod. Phys. **87**, 637 (2015).

[3] I. M. Savukov, S. J. Seltzer, M. V. Romalis, and K. L. Sauer, Tunable Atomic Magnetometer for Detection of Radio-Frequency Magnetic Fields, Phys. Rev. Lett. **95**, 063004 (2005).

[4] B. Patton, O. O. Versolato, D. C. Hovde, E. Corsini, J. M. Higbie, and D. Budker, A remotely interrogated all-optical ^{87}Rb magnetometer, Appl. Phys. Lett. **101**, 083502 (2012).

[5] A. K. Mohapatra, T. R. Jackson, and C. S. Adams, Coherent Optical Detection of Highly Excited Rydberg States Using Electromagnetically Induced Transparency, Phys. Rev. Lett. **98**, 113003 (2007).

[6] T. F. Gallagher, *Rydberg Atoms* (Cambridge University Press, New York, 1994).

[7] J. A. Sedlacek, A. Schwettmann, H. Kübler, R. Löw, T. Pfau, and James P. Shaffer, Microwave electrometry with Rydberg atoms in a vapour cell using bright atomic resonances, Nat. Phys. **8**, 819 (2012).

[8] H. Fan, S. Kumar, J. Sedlacek, H. Kübler, S. Karimkashi, and J. P. Shaffer, Atom based rf electric field sensing, J. Phys. B **48**, 202001 (2015).

[9] J. A. Sedlacek, A. Schwettmann, H. Kübler, and J. P. Shaffer, Atom-Based Vector Microwave Electrometry Using Rubidium Rydberg Atoms in a Vapor Cell, Phys. Rev. Lett. **111**, 063001 (2013).

[10] J. Koepsell, T. Thiele, J. Deiglmayr, A. Wallraff, and F. Merkt, Measuring the polarization of electromagnetic fields using Rabi-rate measurements with spatial resolution: Experiment and theory, Phys. Rev. A **95**, 053860 (2017).

[11] J. A. Gordon, C. L. Holloway, A. Schwarzkopf, D. A. Anderson, S. Miller, N. Thaicharoen, and G. Raithel, Millimeter wave detection via Autler-Townes splitting in

rubidium Rydberg atoms, Appl. Phys. Lett. **105**, 024104 (2014).

[12] D. Barredo, H. Kübler, R. Daschner, R. Löw, and T. Pfau, Electrical Readout for Coherent Phenomena Involving Rydberg Atoms in Thermal Vapor Cells, Phys. Rev. Lett. **110**, 123002 (2013).

[13] H. Q. Fan, S. Kumar, R. Daschner, H. Kübler, and J. P. Shaffer, Subwavelength microwave electric-field imaging using Rydberg atoms inside atomic vapor cells, Opt. Lett. **39**, 3030 (2014).

[14] C. L. Holloway, J. A. Gordon, A. Schwarzkopf, D. A. Anderson, S. A. Miller, N. Thaicharoen, and G. Raithel, Sub-wavelength imaging and field mapping via electromagnetically induced transparency and Autler-Townes splitting in Rydberg atoms, Appl. Phys. Lett. **104**, 244102 (2014).

[15] M. G. Bason, M. Tanasittikosol, A. Sargsyan, A. K. Mohapatra, D. Sarkisyan, R. M. Potvliege, and C. S. Adams, Enhanced electric field sensitivity of rf-dressed Rydberg dark states, New J. Phys. **12**, 065015 (2010).

[16] Y. Jiao, X. Han, Z. Yang, J. Li, G. Raithel, J. Zhao, and S. Jia, Spectroscopy of cesium Rydberg atoms in strong radio-frequency fields, Phys. Rev. A **94**, 023832 (2016).

[17] D. Budker and M. Romalis, Optical magnetometry, Nat. Phys. **3**, 227 (2007).

[18] R. Daschner, H. Kübler, R. Löw, H. Baur, N. Frühauf, and T. Pfau, Triple stack glass-to-glass anodic bonding for optogalvanic spectroscopy cells with electrical feedthroughs, Appl. Phys. Lett. **105**, 041107 (2014).

[19] C. Veit, G. Epple, H. Kübler, T. Euser, P. Russell, and R. Löw, rf-dressed Rydberg atoms in hollow-core fibres, J. Phys. B **49**, 134005 (2016).

[20] C. L. Holloway, J. A. Gordon, S. Jefferts, A. Schwarzkopf, D. A. Anderson, S. A. Miller, N. Thaicharoen, and G. Raithel, Broadband Rydberg atom-based electric-field probe for SI-traceable, self-calibrated measurements, IEEE Trans. Antennas Propag. **62**, 6169 (2014).

[21] The connection of an oscilloscope to the field plates to measure the plate voltage V_C constitutes a change in boundary conditions that will result in a change in t. Also, since impedances are not well defined, V_C will generally not be the same as the voltage measured on the oscilloscope.

[22] D. A. Anderson, A. Schwarzkopf, S. A. Miller, N. Thaicharoen, G. Raithel, J. A. Gordon, and C. L. Holloway, Two-photon microwave transitions and strong-field effects in a room-temperature Rydberg-atom gas, Phys. Rev. A **90**, 043419 (2014).

[23] D. A. Anderson, S. A. Miller, G. Raithel, J. A. Gordon, M. L. Butler, and C. L. Holloway, Optical Measurements of Strong Microwave Fields with Rydberg Atoms in a Vapor Cell, Phys. Rev. Applied **5**, 034003 (2016).

[24] S. A. Miller, D. A. Anderson, and G. Raithel, Radio-frequency-modulated Rydberg states in a vapor cell, New J. Phys. **18**, 053017 (2016).

[25] D. A. Hill, M. Kanda, E. B. Laren, G. H. Koepke, and R. D. Orr, National Institute of Standards and Technology Report No. 1335, 1990.

[26] K. Matloubi, in *Proceedings of the Instrumentation and Measurement Technology Conference, Irvine, CA, 1993* (IEEE, New York, 1993), p. 183.

[27] D. McGloin, M. H. Dunn, and D. J. Fulton, Polarization effects in electromagnetically induced transparency, Phys. Rev. A **62**, 053802 (2000).

[28] S. Bao, H. Zhang, J. Zhou, L. Zhang, J. Zhao, L. Xiao, and S. Jia, Polarization spectra of Zeeman sublevels in Rydberg electromagnetically induced transparency, Phys. Rev. A **94**, 043822 (2016).

[29] L. Zhang, S. Bao, H. Zhang, G. Raithel, J. Zhao, and L. Xia, Nonlinear Zeeman effect, line shapes and optical pumping in electromagnetically induced transparency, arXiv:1702.04842.

[30] C. L. Holloway, M. T. Simons, J. A. Gordon, A. Dienstfrey, D. A. Anderson, and G. Raithel, Electric field metrology for SI traceability: Systematic measurement uncertainties in electromagnetically induced transparency in atomic vapor, J. Appl. Phys. **121**, 233106 (2017).